Article type: Original Paper

Title: Comprehensive analysis of photonic nanojets in 3D dielectric cuboids excited by surface plasmons

Victor Pacheco-Peña[1], Igor V Minin[2], Oleg V Minin[2],and Miguel Beruete[1,3]*

*Corresponding Author: E-mail: miguel.beruete@unavarra.es

[1] Antennas Group - TERALAB, Universidad Pública de Navarra, Campus Arrosadía, 31006 Pamplona, Spain

[2] National Research Tomsk State University, Lenina Ave., 36, Tomsk, 634050, Russia
[3] Institute of Smart Cities, Public University of Navarra, 31006, Pamplona, Spain

In this paper we study the excitation of photonic nanojets (PNJ) in 3D dielectric cuboids by surface plasmons at telecommunication wavelengths. The analysis is done using the effective refractive index approach. It is shown that the refractive index contrast between the regions with and without cuboid should be roughly less than 2 in order to generate jets at the output of the cuboid. The best performance at λ_0 = 1550 nm is obtained when the height of the cuboid is 160 nm producing a jet just at the output interface with a subwavelength resolution of $0.68\lambda_0$ and a high intensity enhancement (×5) at the focus. The multi-wavelength response is also studied demonstrating that it is possible to use the proposed structure at different wavelengths. Finally, the backscattering enhancement is numerically evaluated by inserting a metal particle within the PNJ region, demonstrating a maximum value of ~2.44 dB for a gold sphere of radius $0.1\lambda_0$.

1. Introduction

It is known that the resolution of an imaging system is limited by the diffraction of the electromagnetic waves [1]. To distinguish the subwavelength features of an object, this fundamental limitation must be overcome. Several techniques have been reported enhance the resolution of imaging devices, such as microspherical particles [2]–[4], metamaterials [5]–[7] and plasmonic lenses [8], [9].

Photonic nanojets (PNJs) were proposed some years ago as an alternative to overcome the diffraction limit. PNJs are narrow regions of high electric field concentration produced at the output of micro-scaled cylindrical and spherical (2D or 3D) dielectric particles [10]–[13]. It was demonstrated that PNJs appear just at the output surface of these particles when the refractive index contrast between the dielectric and the background medium was approximately less than 2 [12]. With this configuration, a subwavelength resolution below the diffraction limit can be obtained using a lossless dielectric microsphere [14]–[18]. Other configurations to produce PNJs based on graded index dielectric ellipsoids [19], non-spherical particles [20], [21] and core-shell microcylinders [22] have also been recently reported. The applications proposed encompass backscattering enhancement at microwave wavelengths [23] and optical waveguiding [24]–[26], demonstrating that PNJs are a good alternative to overcome the diffraction limit in a wide spectral range. Recently, we have demonstrated an different way to produce PNJs using 2D/3D dielectric cuboids at terahertz (THz) and sub-THz frequencies,[27]–[29] and also working in reflection mode [30].

Some years ago, it was found that micro scaled dielectric cylinders were able to produce PNJs at optical frequencies when they were excited by surface plasmon polaritons (SPPs) instead of the classical plane wave excitation [31]. This technique has been also applied in the design of plasmonic devices such as Maxwell fish-eye and Luneburg lenses [32], [33], demonstrating the capability to control the focusing properties of a lens by profiling the height

of the dielectric lens in order to obtain the required effective refractive index. Recently, we have used this mechanism combined with 3D dielectric cuboids in the design of a dielectric chain in order to extend the SPP propagation at telecom wavelengths [34]. In this communication, we perform a systematic study of PNJs, both analytical and numerical, by combining 3D dielectric cuboids and SPP excitation at telecommunication wavelengths. The analysis is done in terms of the effective refractive index of the regions with and without cuboids demonstrating that the contrast between effective indices to produce the PNJ just at the output surface of the dielectric must be approximately less than 2. Also, it is shown that the PNJ performance can be engineered by simply changing the height of the dielectric at the operation wavelength, in good agreement with the flat-disk case [31] and also with the recently reported plasmonic lenses [32], [33]. The main advantage of the 3D dielectric cuboids proposed here is that their fabrication is easier, compared with a flat disk and other profiled structures [31]–[33]. Moreover, the influence of the size of the 3D dielectric cuboid and the multi-wavelength response are also studied, demonstrating that the jet can be moved inside or far from the output interface by simply changing the lateral dimensions or the operation wavelength. Finally, the backscattering enhancement of a small metallic sphere is evaluated, demonstrating that this structure can be used for sensing applications at optical frequencies. At difference with our previous work [34] here we perform a complete analysis and design to find the conditions to generate PNJ in a single 3D dielectric cuboid excited by SPPs.

2. Analytical Approach of the SPP Propagation

To begin with, a schematic representation of the proposed structure is shown in Figure 1(a). It consists of a gold film with thickness t = 100 nm on top of a dielectric substrate with a refractive index n = 1.5 (more details of the structure can be found in the supporting information). The dispersive refractive index of gold is modeled following the Johnson and Christy experimental data (shown in the supporting information [35]). A 3D dielectric cuboid of Silicon Nitride

(Si_3N_4) with dimensions $L_x \times L_y \times L_z$ is placed on top of the metal film and the whole structure is immersed in air ($n_1 = 1$). The refractive index of Si_3N_4 is also dispersive in the considered bandwidth (750 - 2000 nm) with values ranging from ~1.97 to ~1.99 between 750 nm and 2000 nm. However, given that this variation is of the order of 10^{-2} within this wide spectral band, a constant refractive index $n_2 = 1.97$ is considered here for simplicity. Numerical simulations are done using the transient solver of the commercial software CST Microwave Studio™. The structure is excited by an extremely narrow waveguide placed at the back of the plasmonic structure (see supplementary information for more details [35]). With this configuration, surface plasmons along *z* are excited at the abrupt interface between the waveguide aperture and air on top of the gold film, as it is shown in Figure 1(b), with the electric field along the *y*- and *z*- axes and magnetic field along the *x*-axis; i.e., a TM wave.

First, we analyze the SPP propagation using the proposed structure. In Figure 1(c), a perspective view of the structure is shown. The SPPs propagate from right to left along the *z*-axis. As it can be inferred, there are two different regions depending of the materials present in the structure [31]: the first region (marked as "I" in the Figure) corresponds to the air-metal interface and the second one (marked as "II" in the Figure) to the air-cube-metal.

As it is known, a metal film can be considered semi-infinite when its thickness is larger than the skin depth [36], [37] which is about 30 nm for gold. Hence, in a real scenario a metal thickness of 100 nm is a good approximation for a semi-infinite slab. This approximation has been extensively used at different wavelengths, such as telecom wavelengths, giving rise to applications such as waveguiding and focusing of SPPs, to name a few [31], [37]–[40]. For completeness we carried out a thorough study to validate this approximation both analytically and numerically (see supplementary information). With the assumption of semi-infinite metal, the analytical complexity of the structure shown in Figure 1 can be largely reduced. The analysis below is done in terms of the propagation constant in each region and from it we extract the

effective refractive index seen by the SPPs (n_{spp}) in each case.

To calculate the effective propagation constant in region I we can use the well-known expression of SPPs excited at a dielectric-metal interface [36], [41]:

$$\beta_{(I)} = k_0 \sqrt{\frac{n_1^2 n_m^2}{n_1^2 + n_m^2}} \tag{1}$$

where k_0 is the wavenumber in free space and n_1 and n_m are the refractive indexes of air and gold, respectively.

To calculate the propagation constant in region II, we must consider three different materials: air, Si_3N_4 and gold [see Figure 1(c)]. It can be obtained after solving this transcendental Equation for $\beta_{(II)}$:[41]

$$\tanh\left(l_y \sqrt{\beta_{(II)}^2 - \varepsilon_2 k_0^2}\right) = -\frac{\varepsilon_m \varepsilon_2 \sqrt{\beta_{(II)}^2 - \varepsilon_1 k_0^2}\sqrt{\beta_{(II)}^2 - \varepsilon_2 k_0^2} + \varepsilon_2 \varepsilon_1 \sqrt{\beta_{(II)}^2 - \varepsilon_2 k_0^2}\sqrt{\beta_{(II)}^2 - \varepsilon_m k_0^2}}{\varepsilon_m \varepsilon_1 \sqrt{\beta_{(II)}^2 - \varepsilon_m k_0^2}\left(\beta_{(II)}^2 - \varepsilon_2 k_0^2\right) + \varepsilon_2^2 \sqrt{\beta_{(II)}^2 - \varepsilon_1 k_0^2}\sqrt{\beta_{(II)}^2 - \varepsilon_m k_0^2}} \tag{2}$$

where the subscripts 1,2 and m refer to air, Si_3N_4 and Au, respectively. Note that the previous expression has an explicit dependence on the height (l_y) of the 3D dielectric cuboid. Hence, we can tune $\beta_{(II)}$ with this parameter. From the previous expressions, it is straightforward to calculate the complex effective refractive index:

$$n_{spp}^{(I),(II)} = \frac{\beta_{(I),(II)}}{k_0} \tag{3}$$

3. Results and Discussion

In this section, we evaluate the performance of the PNJ varying the height and width of the cuboid at a fixed wavelength, the widely used standard telecommunication wavelength λ_0 = 1550 nm [37]–[40]. Later on, we will find the response varying the operation wavelength for fixed cuboid dimensions. Finally, we will insert a small metallic sphere inside the PNJ region to find the backscattering enhancement.

3.1 Photonic nanojet performance

In Figure 2(a) it is shown the variation of $n_{spp}^{(I)}$ between 750 nm and 2000 nm calculated with Equations (1) and (3). As observed, within all the considered bandwidth $\mathrm{Re}\{n_{spp}^{(I)}\}>1$ and it approaches asymptotically unity in the long wavelength limit. This means that SPPs are strongly coupled to the surface of the Au film only for relatively small wavelengths. In particular, at the telecommunication wavelength of 1550 nm, SPPs are weakly coupled. Nevertheless, as it will be seen later, the proposed structure can be engineered to focus the incoming SPPs on a narrow spot of high intensity even at this wavelength.

The analytical results of $n_{spp}^{(II)}$ for $0 < l_y < 500$ nm and $750 < \lambda < 2000$ nm are shown in Figure 2(b,c) respectively. At a given wavelength, increasing the height l_y of the cuboid provokes an increment of both $\mathrm{Re}\{n_{spp}^{(II)}\}$ and $\mathrm{Im}\{n_{spp}^{(II)}\}$, see Figure 2(b,c) respectively. Importantly, $\mathrm{Im}\{n_{spp}^{(II)}\}<<\mathrm{Re}\{n_{spp}^{(II)}\}$ in all considered cases, demonstrating that the structure has low losses.

In Figure 3 we have plotted the real part of effective index contrast between regions I and II, $c=\mathrm{Re}\{n_{spp}^{(II)}/n_{spp}^{(I)}\}$. We have marked three zones depending on the contrast: (i) $c < 1.3$, (ii) $1.3 < c < 1.75$ and (iii) $c > 1.75$. From our previous works, we can foresee that the PNJ will be generated outside, close to the output interface and inside the cuboid when working in region (i), (ii) and (iii), respectively[27].

Based on this, we can now evaluate the performance of the PNJ produced by the proposed structure. From previous works we know that the dimensions of the cuboid should be of the order of the operational wavelength to produce the PNJ at the output surface of the dielectric [27], [28]. Hence, we take $l_x = l_z = \lambda_0 = 1550$ nm and a variable height, l_y. The rest of dimensions of the structure are as shown in Figure 1(a).

With this configuration, we extract from Figure 3 the contrast at 1550 nm as a function of

l_y, see Figure 4(a). The contrast evolves from values close to unity for small l_y to values near 1.9 for large l_y. We have marked in the Figure the three regions [(i)-(iii)] mentioned above, and have selected three representative points: l_y = 100 nm, l_y = 160 nm (we choose this value because we found it is optimal, although is near the limit of the region) and l_y = 350 nm. The numerical results of the power distribution on the *xz*-plane (i.e., just at the surface of the Au film) are shown in Figure 4(b,c,d). It is demonstrated that for l_y = 100nm, where the contrast is ~1.11, the PNJ is moved away from the cuboid and the peak takes place at a focal length (*FL*) of 275 nm ($0.18\lambda_0$), along the *z* axis. For l_y = 160nm where the contrast is 1.35 the PNJ is just at the output surface of the cuboid. Finally when l_y = 350nm, where the contrast is 1.85, most of the power is inside the dielectric cuboid, compared with the case when l_y = 160nm.

To better compare these results, we have plotted the intensity enhancement along the *z*-axis (defined as the power received with and without the cuboid) for the three heights under study. Here it is clearly observed that the maximum is outside the cuboid when l_y = 100 nm while it is at the output interface when l_y = 160 nm. The enhancement at each focal length is ~2.8, ~5.05 and ~3.4 for each height under study, respectively. These values are below those obtained under planewave illumination at THz frequencies [27]. This is due to the fact that the SPPs are not strongly coupled to the surface of the metal film at 1550 nm, as explained before. A larger enhancement could be obtained by designing the structure at smaller wavelengths where the coupling of SPPs to the metal film increases [31]. However, our interest here is to prove that at 1550 nm we can have a relatively large enhancement thanks to the excitation of a PNJ with SPPs since this is the standard telecommunications wavelength [42], [43]. With the results shown, we have successfully demonstrated that the PNJs produced with this configuration are able to enhance more than two times the SPP intensity at the focal length.

For the sake of completeness, the numerical results of the normalized magnitude of the electric field for each height under study are shown in Figure 4(f). Here, the results are

normalized to the maximum of each case. By looking at this plot, the transversal resolution [i.e., full-width at half-maximum ($FWHM_x$) along the x- axis at each focal length] is $1.197\lambda_0$, $0.68\lambda_0$ and $0.43\lambda_0$ for l_y = 100, 160, and l_y = 350 nm, respectively. Note that the best resolution is achieved for the case l_y = 350 nm and it is below the diffraction limit. However, the power of the PNJ decays faster along the propagation direction, as it is shown in Figure 4(e). The best tradeoff between the resolution, enhancement and distance of propagation of the SPP's is achieved when l_y = 160nm.

3.2 Multi-wavelength response

In this section we evaluate the performance of the PNJ produced by the dielectric cuboid at different wavelengths. From the previous study, we fix $l_x = l_z = \lambda_0$ = 1550 nm and l_y = 160 nm.

The results of the refractive index contrast particularized to the case l_y = 160 nm is shown in Figure 5(a). Here the three working zones described in section II (see also Figure 3) are clearly observed: (i) λ > 1600 nm, c < 1.3 so the PNJ is detached from the cuboid; (ii) 1050 < λ < 1600 nm, 1.3 < c < 1.75 and the PNJ happens at the surface of the cuboid, as demonstrated in the previous section; (iii) λ < 1050 nm, c > 1.75 and therefore the PNJ will be inside the cuboid. We have previously analyzed case (ii), and here we evaluate the performance in zones (i) and (iii).

The numerical results of the power distribution on the xz-plane at λ_1 = 800 nm and λ_2 = 1900 nm are shown in Figure 5(b,c). Also, the normalized magnitude of the electric field along the propagation axis at each wavelength is shown in Figure 5(d,e), respectively. It can be observed that the PNJ is generated inside the cuboid when λ_1 = 800 nm and therefore a blurred focus is produced at the output of the structure, as expected [12], [28], [44]. The opposite behavior is observed at λ_2 = 1900 nm where the PNJ is moved far away from the output surface of the cuboid ($FL = 0.2\lambda_2$). For this case a transversal resolution $FWHM_x = 0.97\lambda_2$ is obtained

with an enhancement of ~1.82.

3.3 Scaled 3D dielectric cuboid

We now evaluate the performance of the structure when l_x and l_z are changed. Here, the height of the cuboid is fixed as l_y = 160 nm and the operation wavelength is 1550 nm.

The numerical results of the magnitude of the electric field along the propagation axis are shown in Figure 6 for the cases when the lateral dimensions of the cuboid (l_x and l_z) are scaled by a factor Δ = 1.25, Δ = 1.5 and Δ = 2 (Δ = 1 corresponds to $l_x = l_z$ = 1550 nm). The PNJ is moved far from the surface of the cuboid as the lateral dimensions increase. In each of the considered cases the focal length (*FL*) is $1.35\times10^{-3}\lambda_0$, $5.41\times10^{-3}\lambda_0$ and $0.168\lambda_0$, respectively, in good agreement with our previous findings using a planewave excitation [44]. The magnitude of the electric field along the transversal axis at each *FL* is also shown as insets in Figure 6. It is clearly observed that the transversal resolution is strongly affected by an increment of the size of the cuboid, resulting in a wider focus for higher values of Δ.

The results of the *FL*, $FWHM_x$ and enhancement at the focal length for the structures here studied along with the case with Δ = 1 (discussed in the previous section) are gathered in Table 1. The $FWHM_x$ evolves from $0.68\lambda_0$ to $1.638\lambda_0$ when the cuboid is scaled from Δ =1 to Δ = 2. The enhancement at the focal length is also reduced as the dimensions of the cuboid increase and has a minimum value of 2.37 for Δ = 2. Note that this is still a relatively large enhancement considering that the SPPs are not strongly coupled to the surface of the metal film at the working wavelength. However, in order to work with the best quality of the PNJ in terms of the *FL*, $FWHM_x$ and enhancement, the lateral dimensions of the cuboid should be of the order of the operational wavelength, as it can be corroborated in the same table.

3.4 Backscattering Enhancement

An interesting application of the PNJ is the backscattering enhancement produced when a

small particle is inserted within the PNJ region. The sensing capability of PNJs has been demonstrated using cylindrical/spherical dielectrics and also 3D cuboids under planewave illumination. We can use the structure here proposed and evaluate the backscattering enhancement of metal particles.

A schematic representation of the system is shown in Figure 7(a). The dimensions of the dielectric cuboid are $l_x = l_z = \lambda_0 = 1550$ nm and $l_y = 160$ nm. An electric probe is used at the back of the dielectric cuboid to register the field. A metallic gold (Au) sphere of radius $0.1\lambda_0$ with a dispersive dielectric permittivity following the Johnson and Christy experimental data [35] is introduced within the PNJ region and moved along the optical *z* axis.

With this configuration, the numerical results of the backscattering enhancement (calculated as the ratio between the received electric field with and without sphere) as a function of wavelength (750 - 2000 nm) and sphere position along the *z*-axis [0 - 3000 nm with a step of 77.5 nm ($0.05\lambda_0$)] are shown in Figure 7(b). There are oscillations of the backscattering magnitude that depend on the operational wavelength, in good agreement with previous works [23], [27]. Moreover, it is clearly shown that for wavelengths below 1300 nm, an enhancement of backscattering is no longer possible since the jet falls inside the dielectric cuboid and the intensity of SPPs that reach the sphere is reduced, as demonstrated in Figure 5.

To assess better the performance, the backscattering enhancement at 1550 nm [shown as a dashed line in Figure 7(b)] as a function of the position of the sphere is shown in Figure 7(c). An oscillatory pattern with period of ~$0.6\lambda_0$ is obtained and the first maximum happens at $z \sim 0.45\lambda_0$. At this position, an enhancement of 2.44 dB is obtained, demonstrating the possibility to use this structure for sensing applications. Moreover, it is important to note that an interesting advantage of this structure compared with the structure under planewave illumination [27] is that the metal film provides a platform to place the particle within the PNJ region. Hence the experimental alignment of the particle with the 3D dielectric cuboid is comparatively easier.

4. Conclusions

In this work, the performance of the recently proposed 3D dielectric cuboid to produce PNJ has been evaluated when the structure is excited by SPPs at telecom wavelengths. It has been demonstrated that the height of the cuboid is an important parameter since it changes the effective refractive index of the region where it is present. Moreover, it has been shown that the refractive index contrast between the region with and without the cuboid should be < 2 in order to produce the jet at the output surface of the cuboid, in good agreement with our previous works. The PNJ performance has been evaluated at the telecommunications wavelength of 1550 nm for different heights of the cuboid. This study has been evaluated in terms of FL, $FWHM_x$ and enhancement at the focal position, demonstrating the best response is obtained when the height of the cuboid is l_y = 160 nm with values of $FL \sim 0$, $FWHM_x = 0.68\lambda_0$ and enhancement = 5.05, respectively. The multi-wavelength response has been also evaluated demonstrating that, for a 3 fixed geometry, three operative zones can be distinguished depending on the operational wavelength, with optimal performance in the region where the index contrast is between 1.3 and 1.75. Moreover, the dependence of the PNJ with the lateral dimensions of the cuboid has been studied, demonstrating that the PNJ is moved away from the cuboid as it is enlarged. Finally, the backscattering enhancement has been evaluated by inserting a metal sphere within the PNJ region and shifting its position along the *z*-axis. With this configuration, a maximum enhancement of 2.44 dB has been demonstrated for an Au sphere of radius $0.1\lambda_0$. These results demonstrate that, even when the SPPs are not strongly coupled to the surface of the metal film (used to support the 3D cuboid) it is possible to produce PNJs using dielectric cuboids with a subwavelength focal spot and detect subwavelength metal particles. The results here presented may be interesting in different applications such as sensors, dielectric waveguides with increased SPPs/surface waves propagation distance, plasmonic circuitry

applications, surface optical tweezers, and biosensing.

Supporting Information

Additional supporting information may be found in the online version of this article at the publisher's website.

Figure S1: Real and imaginary part of the complex permittivity of gold.

Figure S2: Real and imaginary part of the complex permittivity of silver.

Figure S3: Schematic representation of the metal film on top of the dielectric substrate used for the SPP excitation and the waveguide used to launch the SPPs.

Figure S4: Analytical results of the effective refractive index for the case of a semi-infinite metal and an IMI structure. Effective index as a function of the metal thickness at the wavelength of 1550nm and numerical results of the E_y-field distribution along the propagation z axis at the wavelength of 1550 nm for the case of an IMI structure with a metal thickness of t = 100 nm.

Acknowledgements This work was supported by the Spanish Ministerio de Economía y Competitividad under contract TEC2014-51902-C2-2-R and partially was supported by the Mendeleev scientific fund of Tomsk State University № 8.2.48.2015. V.P.-P. is sponsored by Spanish Ministerio de Educación, Cultura y Deporte under grant FPU AP-2012-3796. M.B. is sponsored by the Spanish Government via RYC-2011-08221.

Received: ((will be filled in by the editorial staff))
Revised: ((will be filled in by the editorial staff))
Published online: ((will be filled in by the editorial staff))

Keywords: Photonic nanojets, telecom wavelengths, surface plasmons, SPP

References

[1] M. Born and E. Wolf, *Principles Of Optics*, 7th ed. New York: Cambridge University Press, 1999.

[2] Z. Wang, W. Guo, L. Li, B. Luk'yanchuk, A. Khan, Z. Liu, Z. Chen, and M. Hong, "Optical virtual imaging at 50 nm lateral resolution with a white-light nanoscope.,"

Nat. Commun., vol. 2, p. 218, Jan. 2011.

[3] K. W. Allen, N. Farahi, Y. Li, N. I. Limberopoulos, D. E. Walker, A. M. Urbas, V. Liberman, and V. N. Astratov, "Super-resolution microscopy by movable thin-films with embedded microspheres: Resolution analysis," *Ann. Phys.*, vol. 527, no. 7–8, pp. 513–522, 2015.

[4] A. V. Maslov and V. N. Astratov, "Imaging of sub-wavelength structures radiating coherently near microspheres," *Appl. Phys. Lett.*, vol. 108, no. 5, p. 051104, 2016.

[5] J. B. Pendry, "Negative refraction makes a perfect lens," *Phys. Rev. Lett.*, vol. 85, no. 18, pp. 3966–3969, 2000.

[6] R. A. Shelby, D. R. Smith, and S. Schultz, "Experimental verification of a negative index of refraction," *Science*, vol. 292, pp. 77–79, Apr. 2001.

[7] A. Poddubny, I. Iorsh, P. Belov, and Y. Kivshar, "Hyperbolic metamaterials," *Nat. Photonics*, vol. 7, no. 12, pp. 948–957, Nov. 2013.

[8] J. Y. Lee, B. H. Hong, W. Y. Kim, S. K. Min, Y. Kim, M. V. Jouravlev, R. Bose, K. S. Kim, I.-C. Hwang, L. J. Kaufman, C. W. Wong, P. Kim, and K. S. Kim, "Near-field focusing and magnification through self-assembled nanoscale spherical lenses," *Nature*, vol. 460, no. 7254, pp. 498–501, Jul. 2009.

[9] E. T. F. Rogers, J. Lindberg, T. Roy, S. Savo, J. E. Chad, M. R. Dennis, and N. I. Zheludev, "A super-oscillatory lens optical microscope for subwavelength imaging.," *Nat. Mater.*, vol. 11, no. 5, pp. 432–5, May 2012.

[10] Z. Chen, A. Taflove, and V. Backman, "Photonic nanojet enhancement of backscattering of light by nanoparticles: a potential novel visible-light ultramicroscopy technique.," *Opt. Express*, vol. 12, no. 7, pp. 1214–1220, Apr. 2004.

[11] X. Li, Z. Chen, A. Taflove, and V. Backman, "Optical analysis of nanoparticles via enhanced backscattering facilitated by 3-D photonic nanojets.," *Opt. Express*, vol. 13,

no. 2, pp. 526–33, Jan. 2005.

[12] A. Heifetz, S.-C. Kong, A. V Sahakian, A. Taflove, and V. Backman, “Photonic Nanojets.,” *J. Comput. Theor. Nanosci.*, vol. 6, no. 9, pp. 1979–1992, Sep. 2009.

[13] D. McCloskey, J. J. Wang, and J. F. Donegan, “Low divergence photonic nanojets from Si_3N_4 microdisks,” *Opt. Express*, vol. 20, no. 1, p. 128, 2012.

[14] S. Lecler, Y. Takakura, and P. Meyrueis, “Properties of a three-dimensional photonic jet.,” *Opt. Lett.*, vol. 30, no. 19, pp. 2641–3, Oct. 2005.

[15] A. Devilez, N. Bonod, J. Wenger, D. Gérard, B. Stout, H. Rigneault, and E. Popov, “Three-dimensional subwavelength confinement of light with dielectric microspheres.,” *Opt. Express*, vol. 17, no. 4, pp. 2089–2094, 2009.

[16] M.-S. Kim, T. Scharf, S. Mühlig, C. Rockstuhl, and H. P. Herzig, “Engineering photonic nanojets.,” *Opt. Express*, vol. 19, no. 11, pp. 10206–10220, 2011.

[17] L. Zhao and C. K. Ong, “Direct observation of photonic jets and corresponding backscattering enhancement at microwave frequencies,” *J. Appl. Phys.*, vol. 105, no. 2009, 2009.

[18] A. D. Kiselev and D. O. Plutenko, “Mie scattering of Laguerre-Gaussian beams: Photonic nanojets and near-field optical vortices,” *Phys. Rev. A*, vol. 89, no. 4, p. 043803, 2014.

[19] C. Liu, “Ultra-elongayed photonic nanojets generated by a graded-index microellipsoid,” *Prog. Electromagn. Res. Lett.*, vol. 37, no. February, pp. 153–165, 2013.

[20] C. Liu, L. Chang, and L. Yang, “Photonic Nanojet in Non-spherical Micro-particles,” *Proceeding 9th IEEE Int. Conf. nano/micro Eng. Mol. Syst.*, pp. 536–539, 2014.

[21] I. V. Minin, O. V. Minin, and Y. E. Geints, “Localized EM and photonic jets from non-spherical and non-symmetrical dielectric mesoscale objects: Brief review,” *Ann. Phys.*,

vol. 527, no. 7–8, pp. 491–497, 2015.

[22] L. Cheng-Yang and H. Kai-Lung, “Direct imaging of optimal photonic nanojets from core-shell microcylinders,” *Opt. Lett.*, vol. 40, no. 22, pp. 5303–5306, 2015.

[23] A. Heifetz, K. Huang, A. V. Sahakian, X. Li, A. Taflove, and V. Backman, “Experimental confirmation of backscattering enhancement induced by a photonic jet,” *Appl. Phys. Lett.*, vol. 89, no. 22, p. 221118, 2006.

[24] R. M. Cole, Y. Sugawara, J. J. Baumberg, S. Mahajan, M. Abdelsalam, and P. N. Bartlett, “Easily Coupled Whispering Gallery Plasmons in Dielectric Nanospheres Embedded in Gold Films,” *Phys. Rev. Lett.*, vol. 97, no. 13, p. 137401, 2006.

[25] Z. Chen, A. Taflove, and V. Backman, “Highly efficient optical coupling and transport phenomena in chains of dielectric microspheres.,” *Opt. Lett.*, vol. 31, no. 3, pp. 389–91, 2006.

[26] K. W. Allen, A. Darafsheh, F. Abolmaali, N. Mojaverian, N. I. Limberopoulos, A. Lupu, and V. N. Astratov, “Microsphere-chain waveguides: Focusing and transport properties,” *Appl. Phys. Lett.*, vol. 105, 2014.

[27] V. Pacheco-Peña, M. Beruete, I. V. Minin, and O. V. Minin, “Terajets produced by dielectric cuboids,” *Appl. Phys. Lett.*, vol. 105, no. 8, p. 084102, Aug. 2014.

[28] V. Pacheco-Peña, M. Beruete, I. V Minin, and O. V Minin, “Multifrequency focusing and wide angular scanning of terajets,” *Opt. Lett.*, vol. 40, no. 2, pp. 245–248, 2015.

[29] I. V Minin, O. V Minin, V. Pacheco-Peña, and M. Beruete, “All-dielectric periodic terajet waveguide using an array of coupled cuboids,” *Appl. Phys. Lett.*, vol. 254102, pp. 1–6, 2015.

[30] I. V Minin, O. V Minin, V. Pacheco-Peña, and M. Beruete, “Localized photonic jets from flat , three-dimensional dielectric cuboids in the reflection mode,” *Opt. Lett.*, vol. 40, no. 10, pp. 2329–2332, 2015.

[31] D. Ju, H. Pei, Y. Jiang, and X. Sun, “Controllable and enhanced nanojet effects excited by surface plasmon polariton,” *Appl. Phys. Lett.*, vol. 102, no. 17, p. 171109, 2013.

[32] V. N. Smolyaninova, I. I. Smolyaninov, A. V Kildishev, and V. M. Shalaev, “Maxwell fish-eye and Eaton lenses emulated by microdroplets.,” *Opt. Lett.*, vol. 35, no. 20, pp. 3396–8, 2010.

[33] T. Zentgraf, Y. Liu, M. H. Mikkelsen, J. Valentine, and X. Zhang, “Plasmonic Luneburg and Eaton lenses.,” *Nat. Nanotechnol.*, vol. 6, no. 3, pp. 151–5, Mar. 2011.

[34] V. Pacheco-peña, I. V Minin, O. V Minin, and M. Beruete, “Increasing Surface Plasmons Propagation via Photonic Nanojets with periodically spaced 3D dielectric cuboids,” *Photonics*, vol. 3, no. 10, pp. 1–7, 2016.

[35] P. B. Johnson and R. W. Christry, “Optical Constants of the Noble Metals,” *Phys. Rev. B*, vol. 6, no. 12, pp. 4370–4379, 1972.

[36] J. J. Burke, G. I. Stegeman, and T. Tamir, “Surface-polariton-like waves guided by thin, lossy metal films,” *Phys. Rev. B*, vol. 33, no. 8, pp. 5186–5201, 1986.

[37] A. V Krasavin and A. V Zayats, “Silicon-based plasmonic waveguides.,” *Opt. Express*, vol. 18, no. 11, pp. 11791–11799, 2010.

[38] J. M. Steele, Z. Liu, Y. Wang, and X. Zhang, “Resonant and non-resonant generation and focusing of surface plasmons with circular gratings.,” *Opt. Express*, vol. 14, no. 12, pp. 5664–5670, 2006.

[39] L. Feng, K. Tetz, B. Slutsky, V. Lomakin, and Y. Fainman, “Fourier plasmonics: Diffractive focusing of in-plane surface plasmon polariton waves,” *Appl. Phys. Lett.*, vol. 91, no. 081101, pp. 081101–1–3, 2008.

[40] A. Khaleque and Z. Li, “Tailoring the Properties of Photonic Nanojets by Changing the Material and Geometry of the Concentrator,” *Prog. Electromagn. Res. Lett.*, vol. 48, pp. 7–13, 2014.

[41] S. A. Maier, *Plasmonics: Fundamentals and Applications*, First Edit. Springer, 2007.

[42] B. Lauritzen, J. Minář, H. de Riedmatten, M. Afzelius, and N. Gisin, "Approaches for a quantum memory at telecommunication wavelengths," *Phys. Rev. A*, vol. 83, no. 1, p. 012318, 2011.

[43] B. D. Thackray, P. a. Thomas, G. H. Auton, F. J. Rodriguez, O. P. Marshall, V. G. Kravets, and A. N. Grigorenko, "Super-Narrow, Extremely High Quality Collective Plasmon Resonances at Telecom Wavelengths and Their Application in a Hybrid Graphene-Plasmonic Modulator," *Nano Lett.*, vol. 15, pp. 3519–3523, 2015.

[44] V. Pacheco-Peña, N. A. Haritoshin, I. V Minin, O. V Minin, and M. Beruete, "High resolution Terajets via 3D dielectric cuboids at THz frequencies," in *9th International Congress on Advanced Electromagnetic Materials in Microwaves and Optics (METAMATERIALS), 2015*, 2015, no. 1, pp. 463–465.

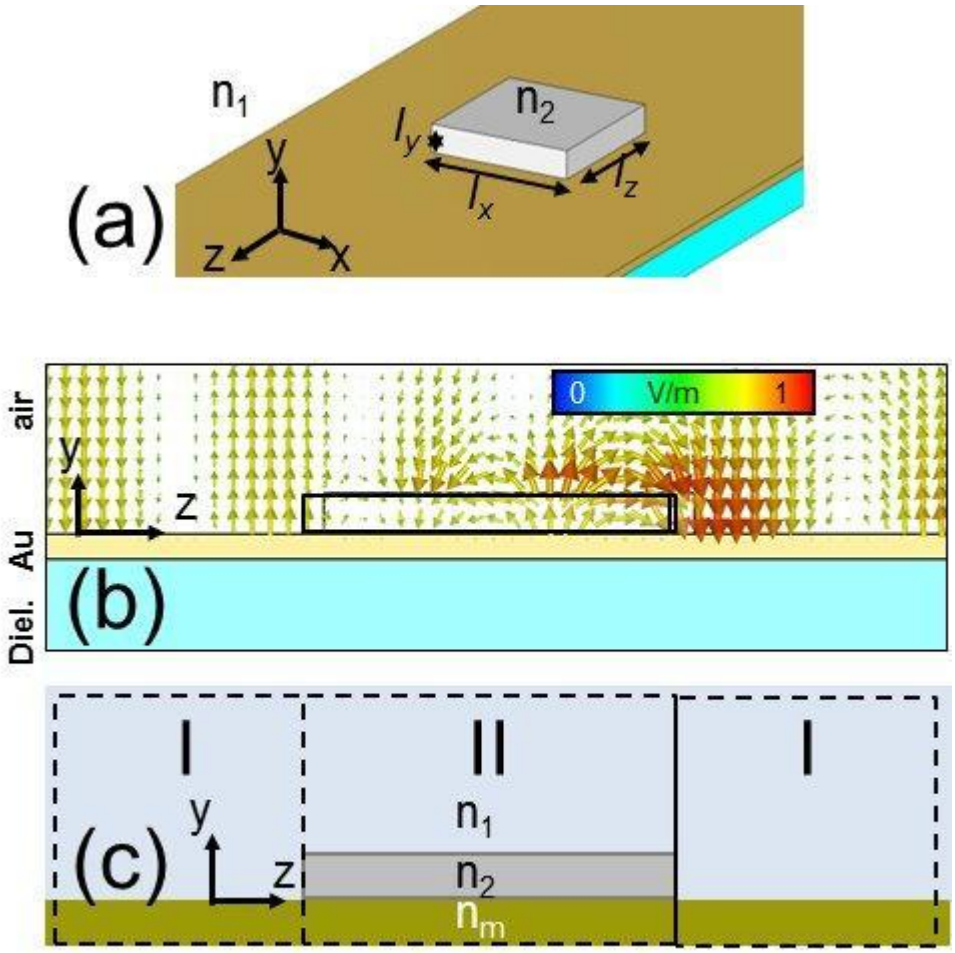

Figure 1. (a) Schematic representation of the structure proposed to produce photonic jets using a 3D dielectric cuboid of Si_3N_4 with a refractive index of ~1.97 and lateral dimensions $l_x = l_z = \lambda_0 = 1550$ nm and a variable height l_y on top of a gold film of thickness $t = 100$ nm laying on top of a dielectric substrate (see inset). (b) Electric field distribution at the operation wavelength (λ_0) on the *yz*-plane. (c) Lateral view of the proposed device showing regions I and II which include the interfaces air-metal (I) and air-cuboid-metal (II), respectively.

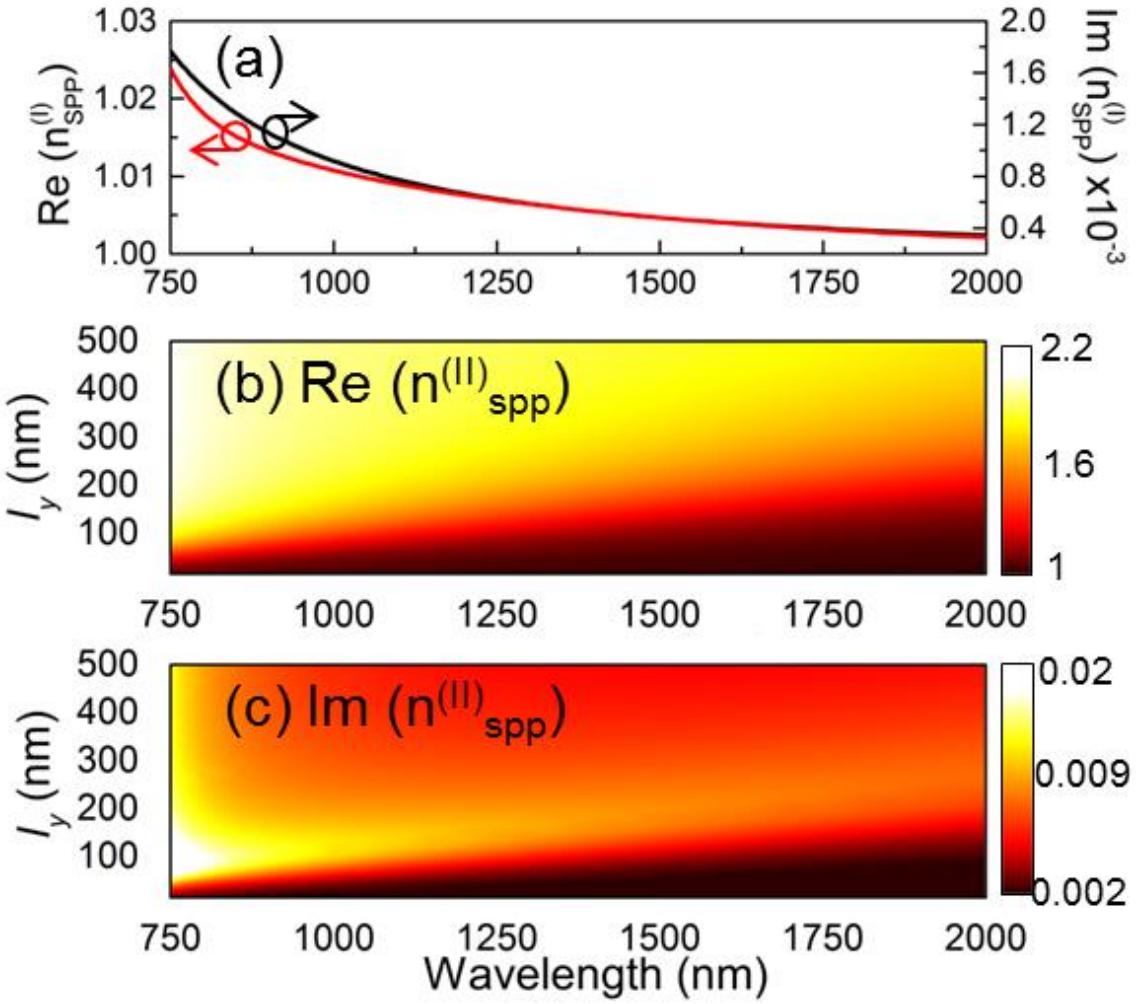

Figure 2. (a) Real (red) and imaginary (black) parts of the effective refractive index for the region I corresponding to the air-Au interface. Real (b) and imaginary (c) part of the effective refractive index in region II as a function of l_y and operation wavelength.

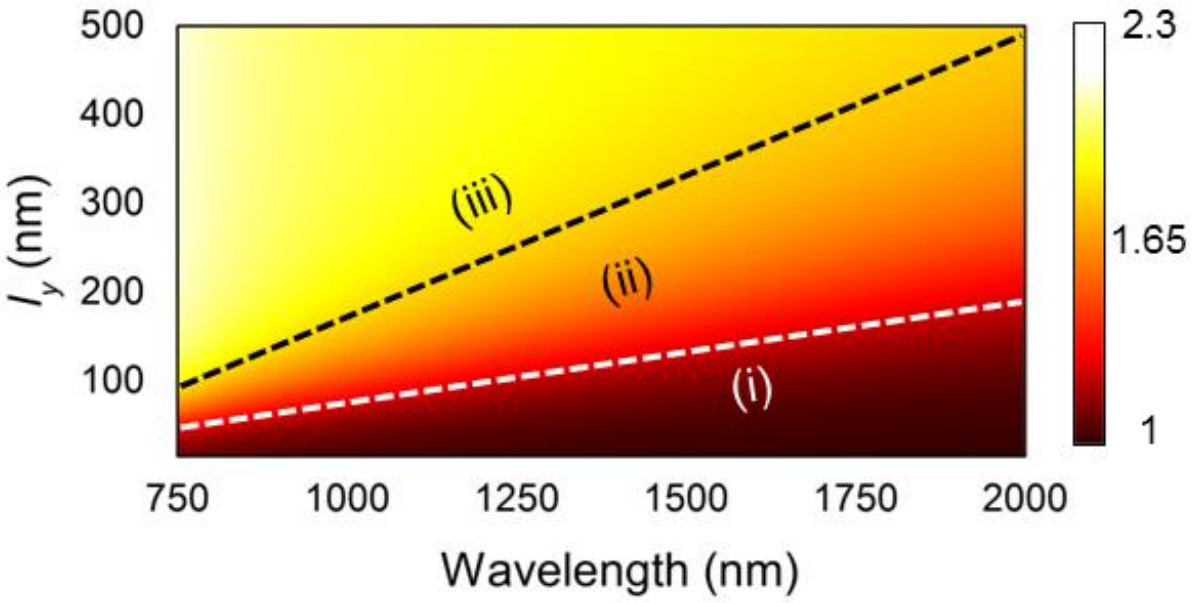

Figure 3. Real part of the refractive index contrast between region II and I as a function of l_y and wavelength. The regions where the contrast is $c < 1.3$, $1.3 < c < 1.75$ and $c > 1.75$ are marked as zones (i), (ii) and (iii), respectively.

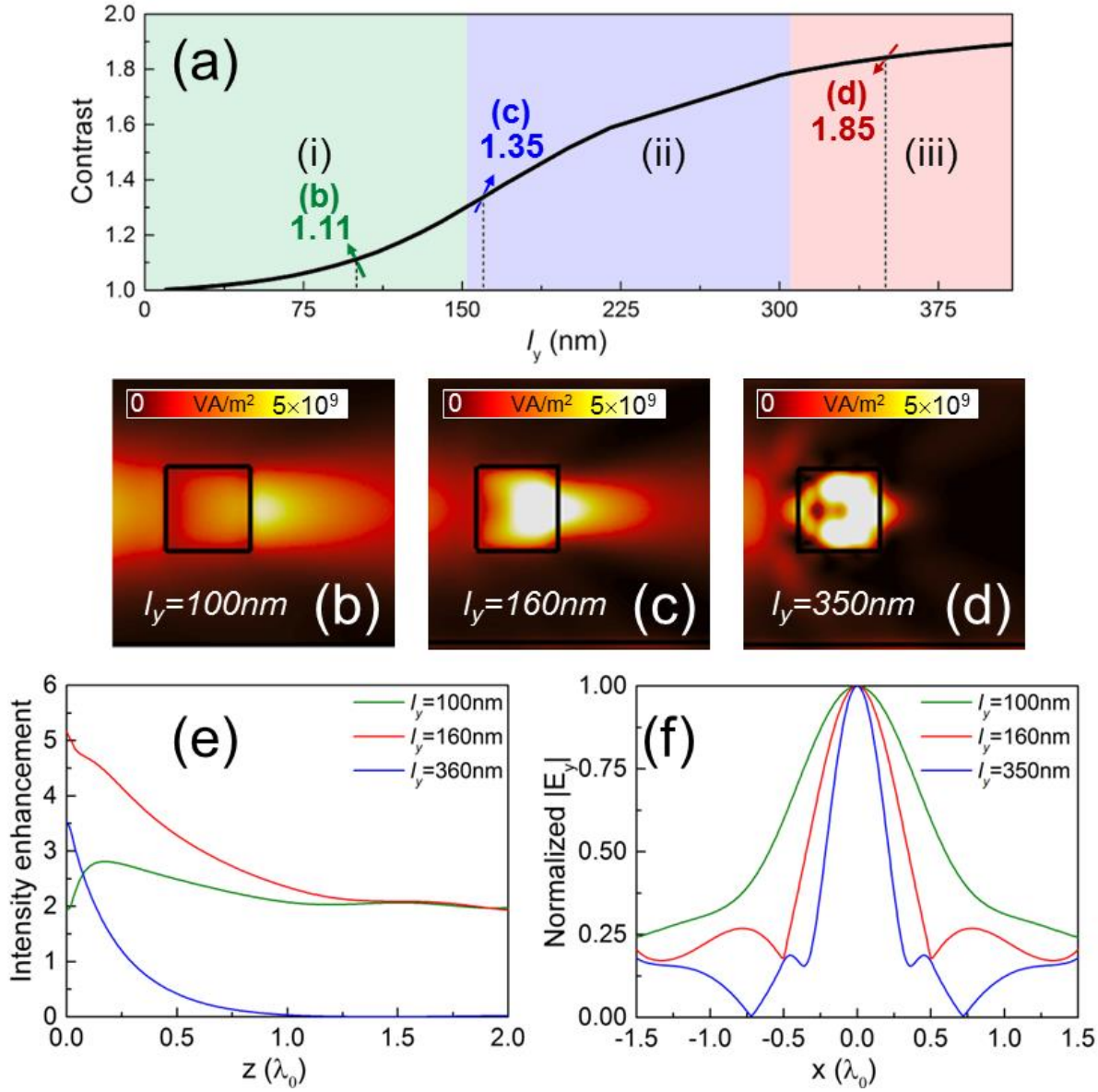

Figure 4. (a) Analytical results of contrast between the effective refractive index of region II and region I. Numerical results of the power distribution on the *xz*-plane just at the surface of the Au film (b,c,d). The regions where the contrast is c >1.3, 1.3 < c < 1.75 and c >1.75 are marked as zones (i), (ii) and (iii), respectively. (e) Numerical results of the intensity enhancement along the *z*-axis (e) and normalized magnitude of the electric field along the *x*-axis at each focal length (f) at the working wavelength of λ_0 = 1550nm for a cuboid with lateral dimensions l_x = l_z = 1550 nm and l_y = 100 nm (green lines), l_y = 160 nm (red lines) and l_y = 350 nm (blue lines).

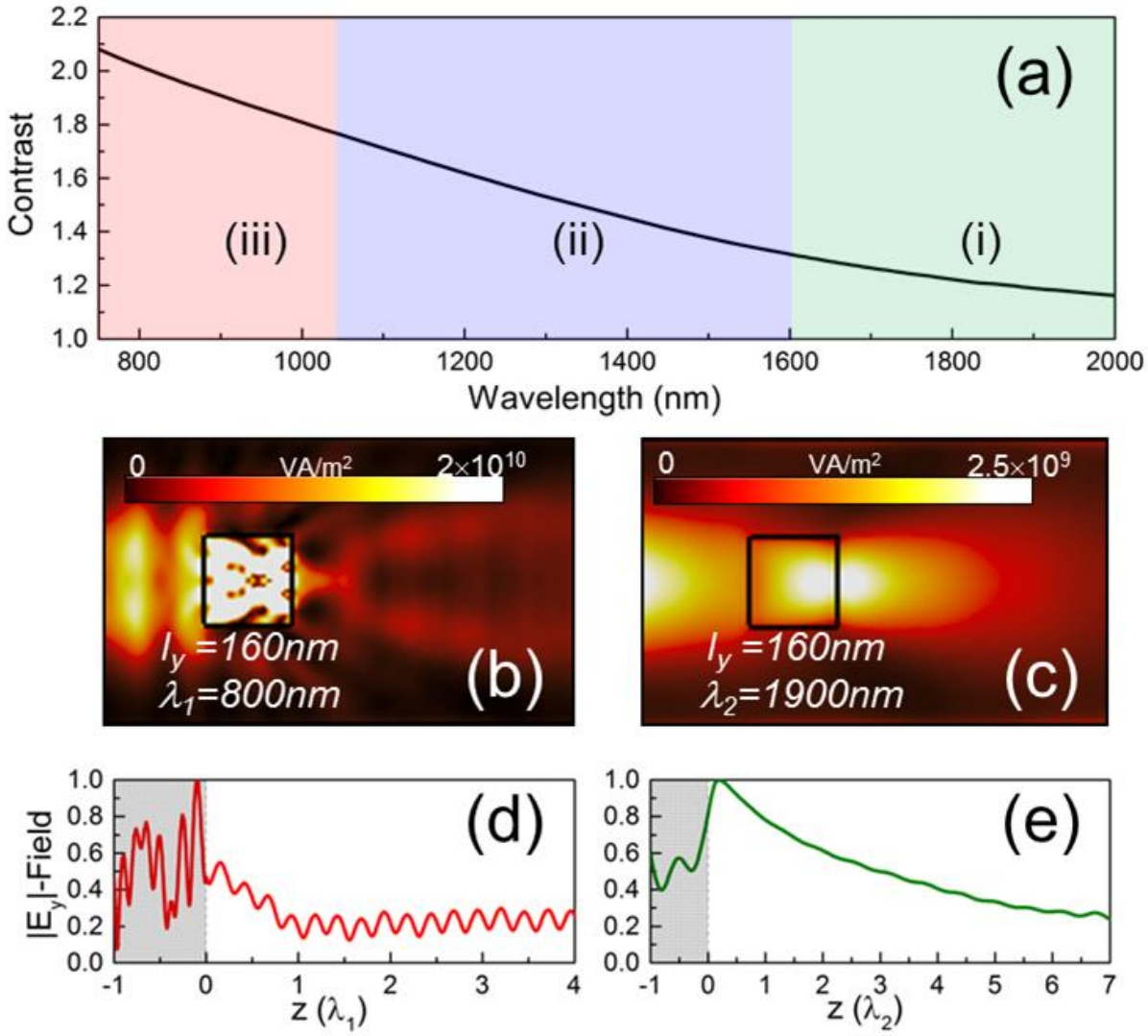

Figure 5. (a) Analytical results of the refractive index contrast between region II and I for a 3D dielectric cuboid with height $l_x = l_z = 1550$ nm and $l_y = 160$ nm. The regions where the contrast is c > 1.3, 1.3 < c < 1.75 and c > 1.75 are marked as zones (i), (ii) and (iii), respectively. Numerical results of the power distribution on the *xz*-plane (b,c) along with the normalized magnitude (normalized at the maximum of each case) of the electric field E_y along the propagation *z*-axis (d,e) at the working wavelength of $\lambda_1 = 800$ nm (b,d) and $\lambda_2 = 1900$ nm (c,e).

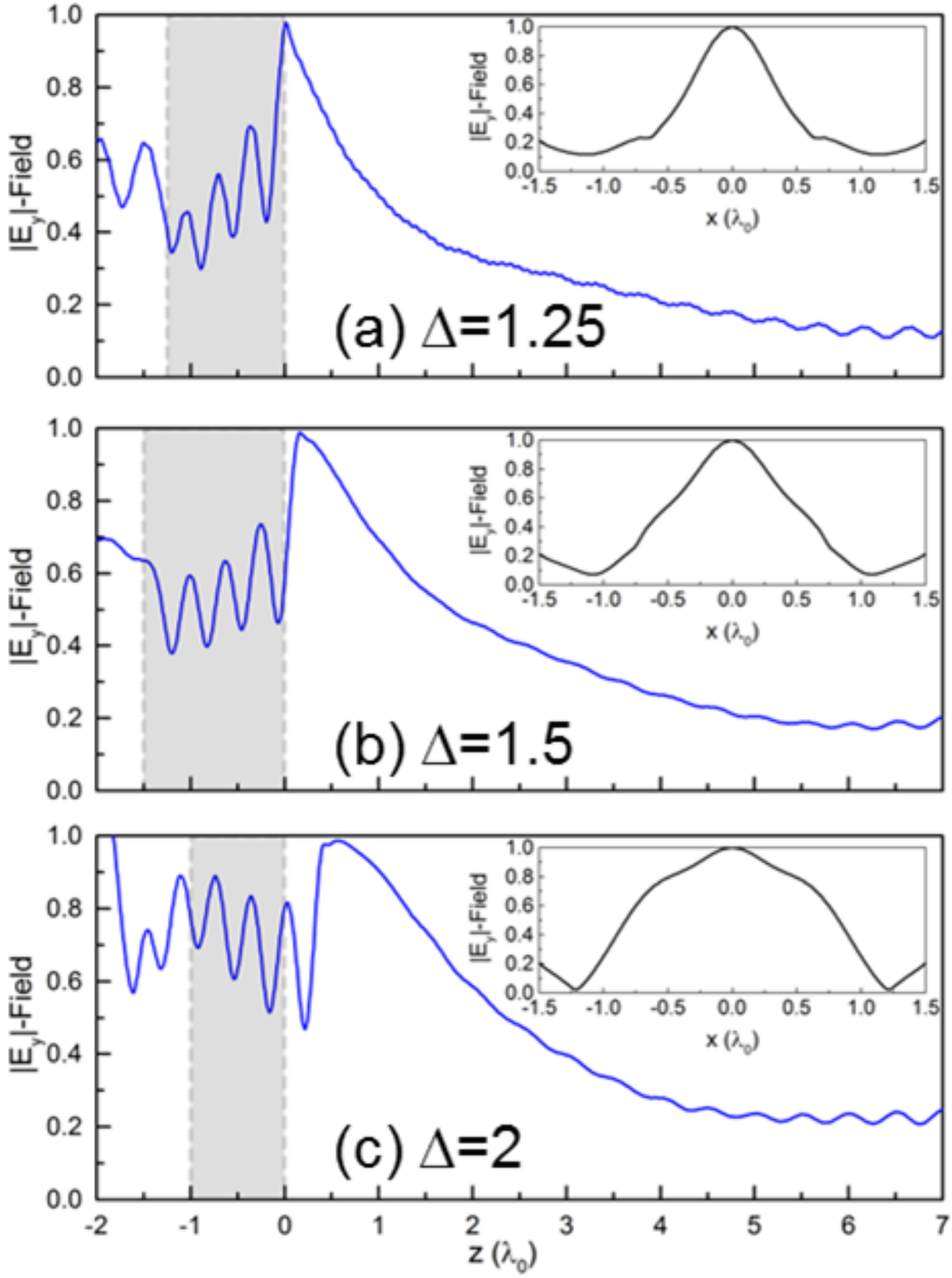

Figure 6. Numerical results of the normalized magnitude of the electric field along the optical *z*- axis for the case of a cuboid with l_y = 160 nm and l_x, l_z scaled by a factor (a) Δ = 1.25, (b) Δ = 1.5 and (c) Δ = 2. The numerical results along the transversal axis at each focal length are shown as insets for each case.

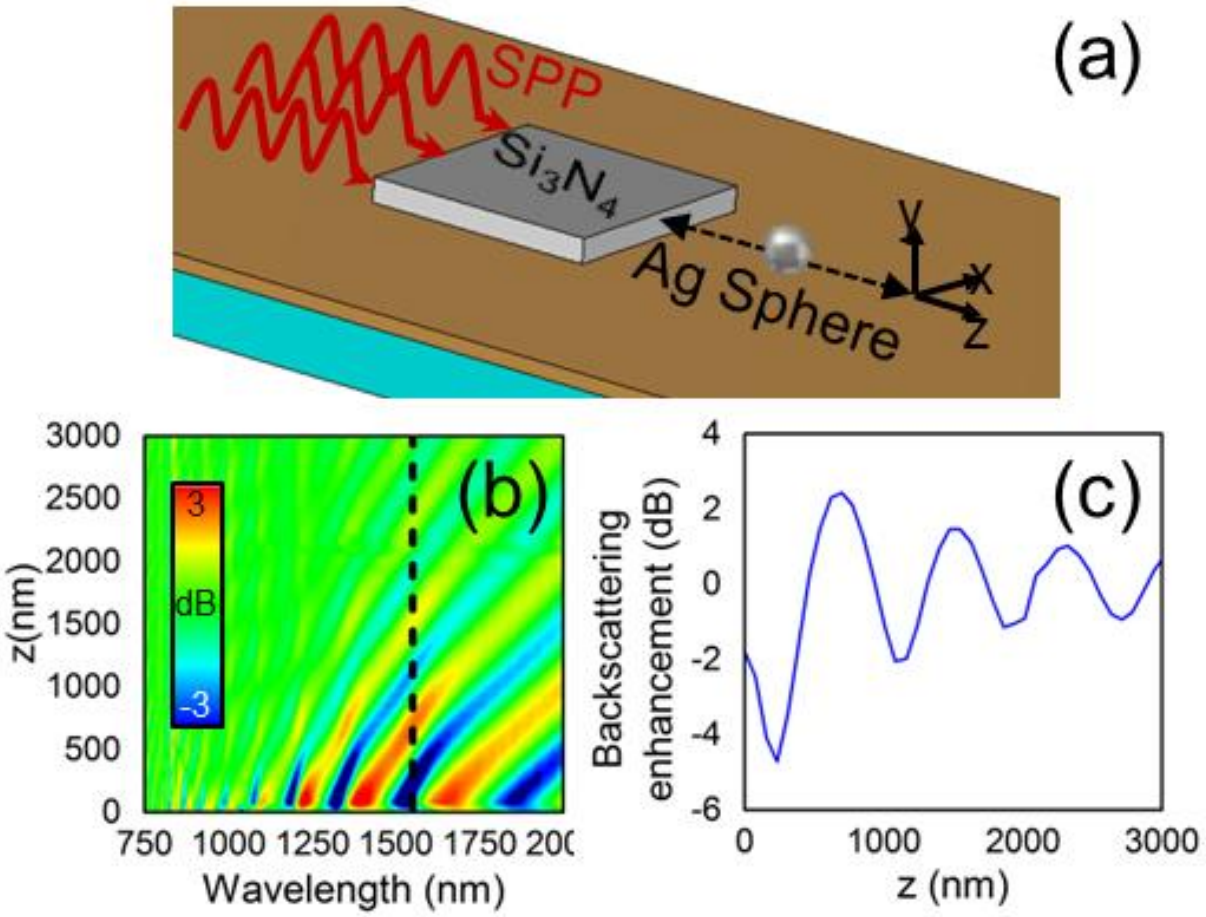

Figure 7. (a) Schematic representation of the system used to evaluate the backscattering enhancement of a metal gold sphere of radius $0.1\lambda_0$ inserted within the PNJ region. (b) Numerical results of the backscattering enhancement as a function of the position of the Au sphere along the *z*-axis and wavelength. (c) Numerical results of the backscattering enhancement at $\lambda_0 = 1550$ nm as a function of the position of the Au sphere [(extracted from the dashed line in (b)].

Table 1. Numerical results of the PNJ performance at the wavelength of 1550nm for a dielectric cuboid with height l_y = 160 nm and lateral dimensions scaled by a factor Δ.

Scale factor (Δ)	FL[a](λ0)	FWHMx[b](λ0)	Enhancement
1	0	0.68	5.05
1.25	1.35×10^{-3}	0.78	4.50
1.5	5.41×10^{-3}	1.096	3.95
2	0.168	1.638	2.37

[a)] *FL* is the focal length; [b)] $FWHM_x$ is the full-width at half-maximum along the *x* axis at the *FL*

Graphical Abstract